

# A Microfluidic Acoustic Metamaterial using Electrowetting: Enabling Active Broadband Tunability

Shubhi Bansal\* and Sriram Subramanian

While acoustic metamaterials provide extraordinary control to manipulate sound waves, their physical realization and applicability are severely impeded by the limited tunability, narrow operational frequency range, and non-compact designs. Integrating liquids with active actuation mechanism in the metamaterials provides broader material and design scope. Active microfluidic techniques for liquid actuation, never used in metamaterials before, will enable active tunability for liquid-embedded metamaterial designs, leading toward a novel class of “microfluidic acoustic metamaterials (MAM).” This work demonstrates deep-subwavelength ultra-compact tunable MAM, consisting of a slit aperture which is tuned by electrically moving a liquid droplet over it using electrowetting-on-dielectric. The proposed design makes MAM inherently multi-stable, and the ability to tune the acoustic field by moving the emission source point provides widescale efficient precision and multiple degrees of freedom. MAM realizes active acoustic switching and amplitude modulation of more than 20 dB and phase modulation from 0 to  $2\pi$  with greater than 80% transmission efficiency analyzed analytically, experimentally, and numerically. MAM also delivers broadband operations ranging from 35 to 45 kHz. This design strategy opens state-of-the-art pathways for automating, tuning, and miniaturizing metamaterials by using microelectromechanical (MEMS) and microfluidic concepts.

membrane-type metamaterials,<sup>[17]</sup> recent work has shown that integrating liquids with the solid structures can dramatically assist reconfigurability. Recently a passively reconfigurable Helmholtz resonator was illustrated, where different volumes of water were filled to tune its free cavity space.<sup>[18]</sup> However, for actively tuning the liquid embedded metamaterial designs, we need active microfluidic techniques for on-chip control of liquid mobility. A number of active microfluidic control mechanisms<sup>[19]</sup> exist in literature like photo-electrowetting, electrophoresis, and surface acoustic waves. These can be used to move microscale droplets in a controlled manner, and have been explored for various applications like lab-on-a-chip,<sup>[20]</sup> printing,<sup>[21]</sup> opto-fluidic lensing,<sup>[22]</sup> and acousto-fluidics.<sup>[23]</sup> However, the field of acousto-fluidics<sup>[24]</sup> has to-date focused only upon manipulating liquid droplets using applied acoustic fields<sup>[25,26]</sup> and not vice versa. Furthermore, there are fabrication challenges in making ultra-compact tunable metamaterial designs, because of the large dimensions, low throughput, bulk


geometries, and huge material costs required for incorporating active control mechanisms. Here, we propose and develop a novel ultra-compact metastructure, which we refer as a metamaterial, with an active actuation mechanism utilizing microfluidics, that will be practically significant and promote a new approach toward microfluidic acoustic metamaterials (MAMs).

In this paper, we design, fabricate, and demonstrate a droplet integrated metamaterial, which derives its tunability from a digital microfluidics based active droplet manipulation technique called electrowetting-on-dielectric (EWOD).<sup>[27–29]</sup> We achieve dynamic control of a deep sub-wavelength slit (dimensions, length =  $0.5 \lambda$  (L), width =  $0.06 \lambda$ , and height =  $0.02 \lambda$ ) for manipulating ultrasound (40 kHz) by using microelectromechanical (MEMS) technology. Ultrathin deep subwavelength metamaterial for example, around  $\lambda/650$  at the frequency of 20.9 kHz ( $\lambda$  denotes the wavelength of sound), where arbitrary patterns were paper-cut by hollow-out patterning on metasurfaces, seldom exist in literature.<sup>[30]</sup> Most of the reported works like ultrasonic meta-lens<sup>[31]</sup> which range within  $\mu\text{m}$  to mm scale are “passive,” but here we propose a novel actively tunable deep subwavelength ultrathin metamaterial (200  $\mu\text{m}$  in thickness, up to  $\lambda/44$ ), establishing a record in comparison with previous works to our best knowledge. MEMS based MAM design paves

## 1. Introduction

Most of the proposed acoustic metamaterials<sup>[1,2]</sup> are based on solid resonating structures such as Helmholtz resonators,<sup>[3,4]</sup> helical labyrinthine structures<sup>[5,6]</sup> and multi-slits<sup>[7,8]</sup> which are passive, and cannot be reconfigured dynamically.<sup>[9,10]</sup> Although a few active reconfigurable acoustic metamaterials<sup>[11]</sup> with different solid materials based actuation and control mechanisms have been proposed, like piezoelectric elements,<sup>[12–14]</sup> multifunctional composites<sup>[15,16]</sup> and electric control in solid

Dr. S. Bansal, Prof. S. Subramanian  
Department of Computer Science  
University College London  
London WC1E 6BT, UK  
E-mail: shubhi.bansal@ucl.ac.uk

 The ORCID identification number(s) for the author(s) of this article can be found under <https://doi.org/10.1002/admt.202100491>.

© 2021 The Authors. Advanced Materials Technologies published by Wiley-VCH GmbH. This is an open access article under the terms of the Creative Commons Attribution License, which permits use, distribution and reproduction in any medium, provided the original work is properly cited.

DOI: 10.1002/admt.202100491

the way to integrate and develop micro-electrode patterns with deep sub-wavelength acoustic structures, for achieving a miniaturized and tunable metamaterial. The building block of the proposed MAM consists of an open slit on an EWOD device, as shown in **Figure 1A**. The figure demonstrates the concept of modulating acoustic transmission through the slit by moving a liquid droplet over it using EWOD. Without any liquid droplet, the acoustic wave transmission from open slit and apertures has been investigated in literature for different slit aspect ratios and lower frequencies (<12 kHz).<sup>[32,33]</sup> However, when the water droplet covers the slit, the impedance mismatch of the liquid–air interface affects the sound transmission, as shown recently by an air bubble based acoustic hologram in water<sup>[34]</sup> where electrolytic bubbles were used to create acoustic holograms because they can provide binary switching due to the impedance mismatch of air–water interface. The large impedance mismatch of air–water interface has also been used to modulate sound waves in superhydrophobic acoustic metasurface designs, where the Cassie–Baxter state of microstructured poly(vinylidene fluoride) membrane enabled confining of acoustic waves in an all-angle and wide spectrum range.<sup>[35]</sup> This work enlightened fluidic applications utilizing giant acoustic impedance mismatch at stable air–water interfaces for waveguiding in fibers for underwater applications. Our work also utilizes this large acoustic impedance mismatch of air–water interface in transmissive air environment. The acoustic energy transmitted at a boundary from water to air and vice versa is very small (<0.1%).<sup>[36]</sup> Thus, the droplet position on the slit determines the effective open slit area which is not blocked by the water–air interface. This open slit area determines the emission point, that is, the effective location of the source, which is determined as the mid-point of open slit length. Unlike most of the metamaterial designs where phase or amplitude is determined by the difference in path travelled by the acoustic wave through different geometric structures, like space-coiling structures, here, the emission point shifts itself to change the acoustic path and correspondingly modulates the phase and amplitude of the transmitted wave. This concept provides a non-complex structure, ease-of-manufacture, active tunability, and multiple degrees of freedom through variable liquid droplet parameters like droplet volume, angle, and position on the slit. By tuning the droplet motion and parameters, we demonstrate multiple MAM operations of tunable binary acoustic switching, active amplitude modulation, and phase modulation, experimentally and through simulations. We also present an analytical theoretical model that fits our MAM design to determine the transmission efficiency which is found to be greater than 80%. We further analyze the broadband dynamics of MAM. The ability to tune and modulate acoustic waves by controlling a liquid droplet on a deep-sub-wavelength metamaterial, opens a new paradigm of possibilities toward miniaturized dynamic MAMs with numerous versatile applications like holography and acoustic imaging.

## 2. Results

### 2.1. Implementation and Operation of MAM

Implementing dynamic tunability and programmability on deep sub-wavelength acoustic structures has numerous engineering

challenges like small size, precision control with subwavelength resolution, thin form factor, geometrical complexity, low efficiency, interference between actuating field like voltage and the acoustic field, and compatibility with standard fabrication techniques. Inspired by MEMs devices, the MAM device is fabricated (device fabrication process is explained in Figure 1D and Experimental Section) on a transparent and flexible ITO (indium tin oxide) coated PET (polyethylene terephthalate) substrate which provides both transparency and conductivity for liquid actuation. The deep subwavelength slit, optimized to support both the acoustic transmission and droplet motion, is made using a laser cutter. A set of actuation and grounding electrodes are patterned on either side of the slit to sequentially actuate and direct the droplet motion over the slit (see Figure S1, Supporting Information). The electrode designs optimized to move droplet over the slit are discussed in the Supporting Information. We use 150 V DC-voltage driving signal for moving the deionized water droplet over the slit (Video S1, Supporting Information). We observe the metamaterial operation of acoustic switching and amplitude modulation of sound realized here experimentally using droplet (i.e., air–water interface) motion (Figure 1B). The acoustic phase can also be modulated in a similar fashion. Figure 1C shows the phase map that illustrates a  $-\pi$  to  $+\pi$  phase shift over a wavelength achieved by droplet motion, when the emission point shifts itself from  $-2$  to  $2$  mm along the 4.5 mm open slit aperture using simulations. Since the electric field is only required to move the droplet to a new position and not to keep it in that location, the electric field ( $V_{\text{OFF}}$ ) can be turned OFF before turning ON the acoustic field ( $S_{\text{ON}}$ ), thereby avoiding any interference between the acoustic and electric field. This also shows that MAM is inherently multi-stable because it holds the droplet position and MAM's state stably till an electric field is applied to move the droplet to a new position. For maintaining MAM operation for longer durations, the liquid can be supplied through a reservoir-on-chip to the required position on the MAM by microfluidic operations like droplet generation, moving, or merging.<sup>[20,37,38]</sup>

### 2.2. Active Acoustic Switching

To quantify the switching dynamics, we move a deionized water droplet (25  $\mu\text{L}$ , 90°) on the fabricated metamaterial slit using 150 V actuation voltage, to attenuate and alter the transmitted acoustic field. The schematic in **Figure 2A** illustrates the cut-plane and cut-line along  $x$ – $z$  plane and  $x$ -axis for measuring the field. Figure 2B plots the transmission spectra of 40 kHz sound wave through the device in  $x$ – $z$  plane, measured from 15 mm ( $\approx 1.74 \lambda$ ) above the substrate. The transmitted sound amplitude decreases by more than 20 dB, when the droplet covers the slit, demonstrating MAM behavior as a tunable acoustic switch. The corresponding simulations are in close agreement with the experimental results. For quantitative comparison, the field was measured on a line 15 mm ( $1.74 \lambda$ ) above the slit ( $z = 0$ ) both without and with the droplet as plotted in Figure 2C (blue and red lines respectively). Here, the experimental and simulated pressure distribution for acoustic switching shows a significant pressure drop (>20 dB). Thus, MAM act as a binary acoustic switch, which is tuned from open (or ON) switch state to covered (or OFF) switch state by moving a liquid droplet over the slit.

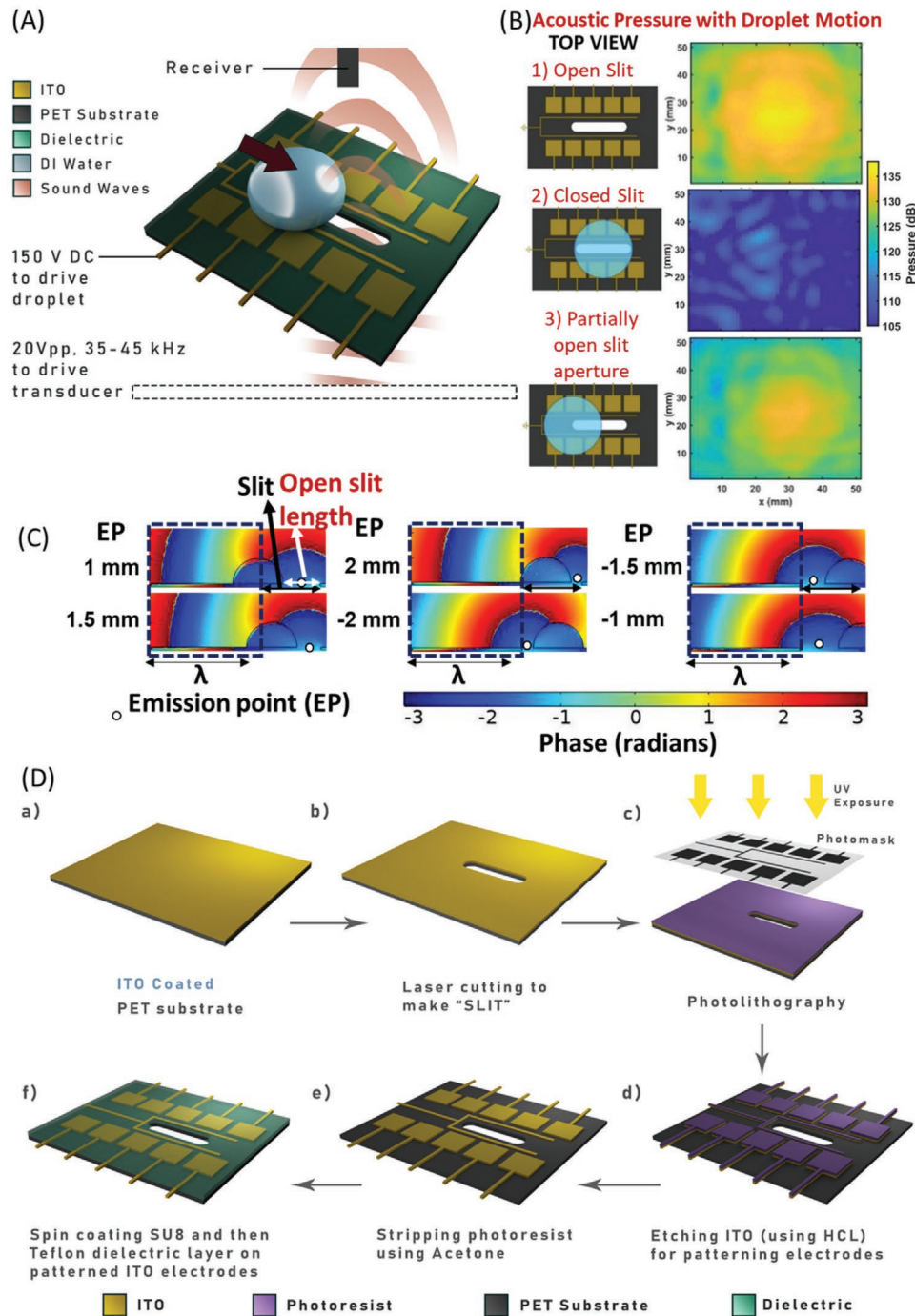


**Figure 1.** Main elements of the postulated dynamically tunable MAM. A) A geometrical description of MAM consists of a droplet on a sub-wavelength slit combined with electrowetting-on-dielectric (EWOD) device driven by input voltage signal. The droplet motion changes the effective open slit length, thereby tuning the emission point for transmitting the acoustic field. B) Schematic illustrations of the top view of the device for different droplet positions, and corresponding measured acoustic pressure maps for 40 kHz wave, captured at a  $x$ - $y$  plane 15 mm ( $1.74 \lambda$ ) above the substrate (slit center is at center of  $x$ -axis and  $y$ -axis here, that is, (25,25) mm position). C) Simulated acoustic phase map for 40 kHz frequency varies from  $-\pi$  to  $+\pi$  as a 25  $\mu$ L droplet moves to cover different positions, thereby causing different emission points ( $-2$  to 2 mm) on the slit. Here, the black arrows mark the slit without any droplet while the white arrows determine the open slit aperture, that is, width of the source, and the white circles depict the emission point. The dotted blue rectangle marks the acoustic wavelength ( $\lambda$ ). D) Schematic illustration of the process flow for fabrication of microfluidic acoustic metamaterial (MAM). a) ITO (metal) coated PET substrate, b) laser cutting to make slit, c) photolithography to pattern electrodes, d) etching metal, e) stripping photoresist, and f) spin coating dielectric layers (SU8 and Teflon; see Experimental Section and Video S2, Supporting Information for details).

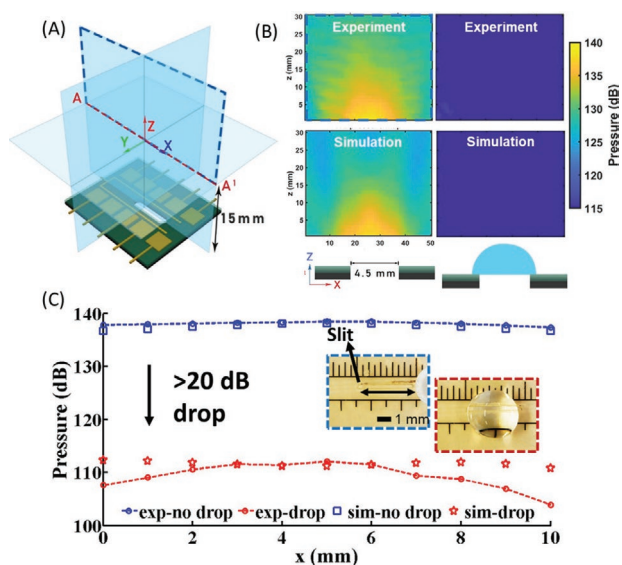


**Figure 2.** Binary switching dynamics of MAM. A) Schematic of the device with  $x$ - $z$  cut plane and AA' cutline marked with dotted line for better visualization of the captured acoustic data. All measurements are taken from 15 ( $\approx 1.74 \lambda$ ) mm above the substrate, that is, 15 mm above substrate correspond to  $z = 0$  mm for  $x$ - $z$  plane. B) Measured pressure field distribution in  $x$ - $z$  plane (top-left) without any droplet, switch ON ( $S_{\text{ON}}$ ) and (top-right) with 25  $\mu\text{L}$  droplet positioned at center of the slit, switch OFF ( $S_{\text{OFF}}$ ; bottom) Calculated pressure field distribution using simulations for above mentioned conditions. Schematic images depict the droplet position on the slit showcasing the open slit and the closed slit. Color bars represent normalized pressures (dB scale). C) Measured and simulated acoustic pressure plotted along slit length (i.e.,  $x$ -axis in (A)) for 10 mm length (slit center is at 5 mm here), without and with the droplet on the slit marked with blue and red lines, respectively. The inset shows the experimental images captured without and with the droplet on the slit.

### 2.3. Spatial Ultrasound Modulation via Droplet Manipulation

The directed motion of the droplet on the subwavelength slit could laterally shift the emission point of the acoustic wave and change the open slit aperture, unlike the acoustic switching where the full slit is covered by the droplet. The two tunable parameters which change with droplet position are- 1) open slit length, that is, slit aperture or width of source and 2) the emission point, which is considered here as  $x$ -position of the center of the open slit aperture (see Figure S2, Supporting Information). We realize the acoustic wavefront manipulation by varying both these factors, which enables MAM to work as a spatial field modulation device capable of simultaneous amplitude modulation and phase modulation. Simultaneous phase and amplitude modulation allows additional degrees of freedom which leads to a marked simplification of the metasurface design process.<sup>[39]</sup>

#### 2.3.1. Amplitude Modulation

Unlike switching, here we measure the space discretized acoustic pressure map for an open slit (length  $\approx 4.5$  mm), and with a droplet (15  $\mu\text{L}$ ,  $90^\circ$ ) positioned along the left end of

the slit to cover 3 mm of slit length, implying 1.5 mm open slit aperture. We measured the acoustic field for  $x$ - $z$  and  $x$ - $y$  plane simultaneously for same droplet positions to realize 3D acoustic transmission field dynamics (see Figure 3A). The shift in the acoustic field without and with the droplet at left end of slit, clearly demonstrates the spatial shift and lateral confinement of the acoustic field in 3D space (marked with dotted red line). The experimentally derived pressure field is in a good agreement with the simulation. Thus, the droplet acts as a barrier to cause 3D spatial modulation of the acoustic field. The experimental images for droplet motion and different droplet positions on the slit have been captured, as shown in Figure S3, Supporting Information. The simulated acoustic field without any device, with MAM device without any droplet, and when the droplet is partially blocking MAM slit, is plotted in Figure 3B for a line along  $x$ -axis and 15 mm above the substrate, demonstrating the shift in peak pressure amplitude and its position.

To study the effect of the open aperture, we capture the transmitted field at a point  $(x, z) \approx (0, 0)$  when we move a 25  $\mu\text{L}$  droplet along the left end of the slit providing different open apertures (3.8 to 4.4 mm) both experimentally and by simulations (Figure 3C). We observe that as the droplet moves to cover more area on the slit, the transmitting sound amplitude reduces. The simulation shows similar trend, that is, decrease in sound amplitude (dB) with decrease in open slit aperture. This is attributed to higher reflection occurring from less opened slit aperture, similar to an acoustic barrier.<sup>[40]</sup> Thus, the metamaterial can modulate the transmission amplitude (up to 20 dB) by tuning the droplet position on the slit via electrowetting.

The above-mentioned measurement was done at a single point, however, to determine the spatial behavior of the field based on width of the source, we simulated acoustic pressure over a line 15 mm ( $\approx 1.74 \lambda$ ) above the substrate for different emission points. First, we moved the droplet (25  $\mu\text{L}$ ,  $90^\circ$ ) along the slit length (0 to 4.5 mm), such that the open slit aperture varies from 1 to 4 mm in steps of 1 mm. We observe that the peak transmitted amplitude, measured over a line 15 mm ( $\approx 1.74 \lambda$ ) above the substrate, decreases with a decrease in open slit length (Figure 3D), similar to the constant point measurement above. The position of obtaining these peaks also shifted proportionally with the shift in the emission point. We fixed the emission point, to study the effect of only the width of source, by simulating the case where two droplets each at both ends of the slit move such that the emission point is maintained at the center of the slit. We observed same peak-amplitude values for different slit open slit aperture as plotted in Figure 3D for two drops. This shows that the peak-amplitude value is affected only by the open slit aperture, that is, the width of the source, and not by the emission point. However, the  $x$ -position for obtaining peak amplitude value shifts proportionally with the emission point, implying spatial transformation of the transmitted field with the droplet.

**Analytical Modeling.** While a theoretical model<sup>[41]</sup> to calculate the transmission coefficient for a wave normally incident on deep sub-wavelength rectangular slit was recently proposed, the model assumes one of the slit dimensions to extend to infinity. Here, we extend the model to consider a 3D slit, with length  $-l/2$  to  $l/2$ , width  $-w/2$  to  $w/2$  and depth  $h$ . The transmission

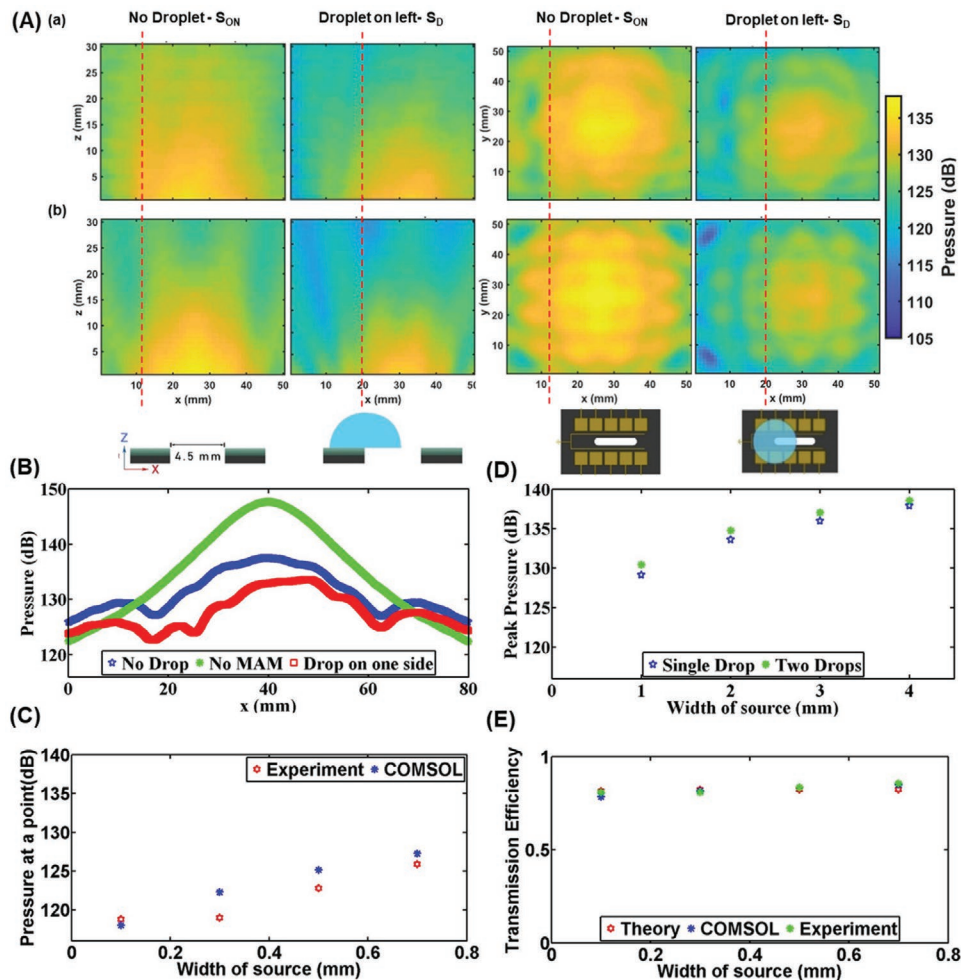


**Figure 3.** Spatial ultrasound field amplitude modulation using MAM. A) The acoustic pressure field distribution by a) measurement in (left-half)  $x$ - $z$  planes and (right-half)  $x$ - $y$  planes each for without any droplet, that is, switch ON ( $S_{ON}$ ) and with 15  $\mu\text{L}$  droplet positioned at left end of the slit, acquiring 3 mm of slit length, thereby displacing the transmitted field ( $S_D$ ). b) Simulated pressure field maps for above mentioned conditions. Schematics depict slit without a droplet, and with droplet on left, in the  $x$ - $z$  and  $x$ - $y$  planes. Color bars represent normalized pressures (dB scale). B) Simulated pressure field without any device, with MAM device without any droplet, and when the droplet is placed on one side such that the width of the source is 2 mm, plotted along slit length (i.e.,  $x$ -axis such that slit center is at 40 mm). C) Experimental and simulation-based quantization of the 40 kHz acoustic pressure at a specific point ( $x, y, z$ )  $\approx$  (0,0,0) to realize the effect of width of the source ( $\approx$ 0 to 0.8 mm). D) Peak pressure amplitude measured over a line 15 mm ( $\approx 1.74 \lambda$ ) above the substrate plotted as a function of width of the source. E) Transmission efficiency plotted with respect to the width of the source solved theoretically, experimentally and by simulations. All measurements are taken at 15 mm ( $\approx 1.74 \lambda$ ) which correspond to  $z = 0$  mm for  $x$ - $z$  plane.

coefficient is found by solving for continuity of pressure and velocity at boundaries as,

$$T = \frac{4Qe^{ihk_0}}{(Q+1)^2 - (Q-1)^2 e^{2ihk_0}} \quad (1)$$

where  $Q = \frac{k_0}{\pi w l} \iint_{-\infty}^{\infty} \frac{(1 - \cos(l\alpha))(1 - \cos(w\gamma))}{\gamma^2 \alpha^2 \sqrt{k_0^2 - \alpha^2 - \gamma^2}} d\alpha d\gamma$ , where

$\alpha$  and  $\gamma$  are the wave-vectors in  $x$  and  $y$  direction respectively (details in Supporting Information). The waves transmission through the aperture is adequately described by this model, as revealed by the good match between the experiments, simulations, and calculations (Figure 3E). The transmission efficiency for extreme subwavelength width of source ( $\approx 0$  to 0.8 mm)

was found to be greater than 80%, implying an efficient MAM operation.

### 2.3.2. Phase Modulation

To investigate the acoustic phase modulation, we capture the phase map when there is no droplet on the MAM and when a droplet (15  $\mu\text{L}$ ,  $90^\circ$ ) is positioned on the left side of the slit (covering 3.7 mm slit length). We observe that the wave-phase shifts toward right compared to the phase-map when no droplet was there (Figure 4A). There is a good agreement between the experimental and simulation results. The phase shift corresponds to droplet movement, that is, the motion of air-water interface which in turn moves the emission point. Thus,

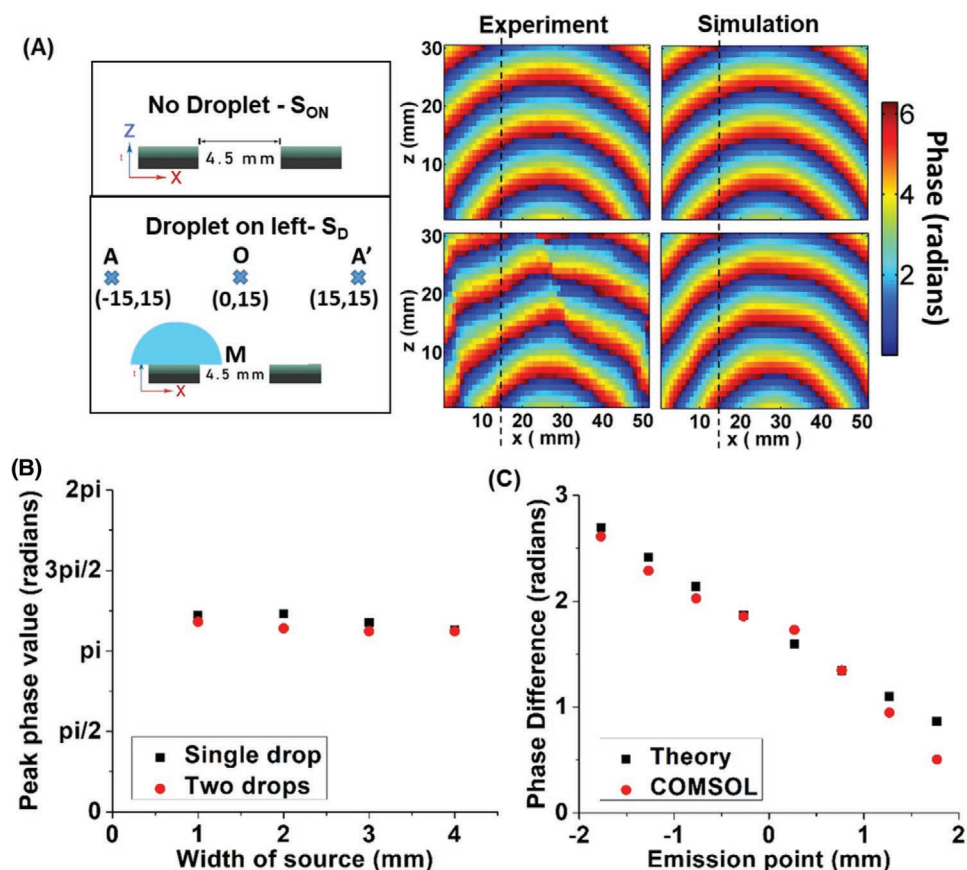


**Figure 4.** Active phase modulation using MAM. A) The spatial distribution of the phase of the acoustic field predicted by (left) experiments and (right) simulations, each for (top) no droplet and (bottom) droplet (volume 15  $\mu\text{L}$ ) covering 3.7 mm slit length. The dotted black line marks the phase wavefront on  $x$ -axis corresponding to acoustic field  $S_{\text{ON}}$  for the no droplet case and the displaced field ( $S_{\text{D}}$ ) when the droplet is on left end of the slit. Color bars represent the acoustic wave phase from 0 to  $2\pi$ . B) The peak phase value calculated on a line ( $1.74 \lambda$  above the slit) for different open slit apertures obtained by moving droplet in following two cases- a single droplet (black square marker) moving on the slit and two drops (red circle marker) each moving equally at each end of the slit to maintain a consistent emission point at the slit center. C) The phase difference between two points on the wavefront (O, A shown in schematic of (A)) calculated using simulations and theoretical calculations plotted with respect to different emission points. The phase difference shifts proportionally with the emission point, enabling active phase modulation.

changing the emission point changes the phase of the acoustic wave, demonstrating metamaterial capability for active phase modulation.

To determine the phase of the field based on emission point, we simulate acoustic phase over a line 15 mm ( $\approx 1.74 \lambda$ ) above the substrate for different emission points. Unlike the amplitude, the peak phase value calculated on a line ( $1.74 \lambda$  above the slit) does not show any variation with the aperture width (Figure 4B), because the acoustic wavefront is travelling the same distance for all widths. However, the  $x$ -position of peak phase shifts proportionally with the shift in emission point  $x$ -position. Like the section above, we also simulated two drops each at both ends of the slit to check the effect of width of source on peak phase value (Figure 4B). We observe that though the peak phase value does not change with the width of the source, but it shifts spatially with the position of the source. So, we simulated the path difference between two points in space for different emission points; and we observed that the spatial wave-phase can be actively tuned from  $-\pi$  to  $+\pi$  by manipulating the effective location of the source (Figure 4C).

The theoretical phase difference ( $\Delta\phi$ ) between two points in space can be predicted as  $\Delta\phi = 2\pi \cdot \Delta x / \lambda$ , where  $\Delta x = ((x_1 - x_2) \bmod \lambda)$  is path difference between two points on the wavefront from the emission point and  $\lambda$  is the wavelength of the source, that is, 8.6 mm. The analytically calculated phase difference matches with the simulated wave-phase value thereby verifying the active phase modulation behavior in the simulations. The proposed metamaterial allows on-demand tunability the acoustic phases by actuating and moving the liquid droplet to and from specific positions on the slit. In an electrowetting platform, one can move liquid droplets at speeds of up to  $40 \text{ mm s}^{-1}$ ,<sup>[42]</sup> supporting applications such as holography,<sup>[43]</sup> imaging,<sup>[44]</sup> and acoustic communication,<sup>[45]</sup> which will all benefit from high-speed tunability.

#### 2.4. Effect of Other Tunable Droplet Parameters

MAM provides multiple degrees of freedom through variable control parameters like droplet contact angle, volume, and

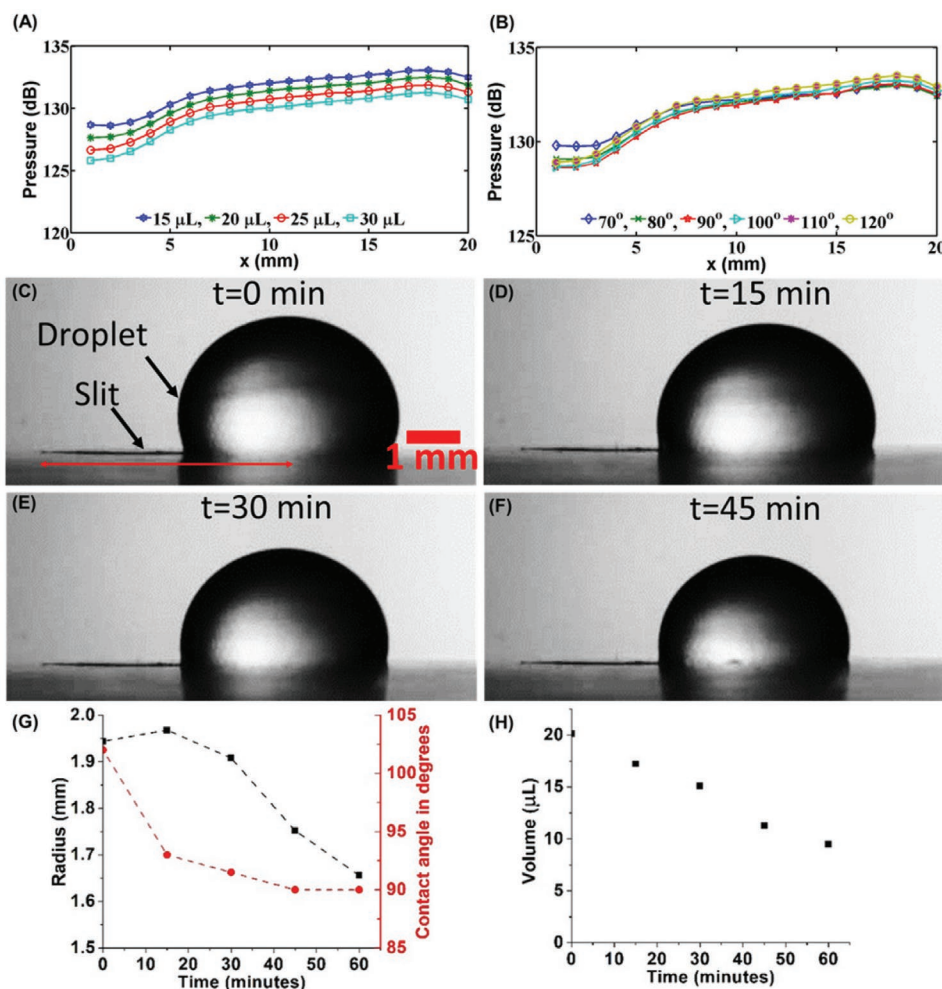


**Figure 5.** Effect of tunable droplet parameters on MAM operation. The variation in acoustic pressure plotted along slit length (a 20 mm line along x-axis, such that the slit center is at 10 mm) for 1.5 mm open aperture or width of the source with  $x = 1.5$  mm emission point, for different A) droplet volumes ranging from 15 to 30  $\mu\text{L}$  in steps of 5  $\mu\text{L}$  for constant contact angle ( $90^\circ$ ); and B) droplet contact angles ranging from  $70^\circ$  to  $120^\circ$ , in step of  $10^\circ$ , for constant radius (1.9 mm). Above  $70^\circ$ , the acoustic pressure for all the angles overlaps. C–F) Experimental images of the side view of the droplet on the slit captured using a high-speed camera. It shows the temporal evolution of the droplet (volume 20  $\mu\text{L}$ ) sitting in constant acoustic pressure (40 kHz) over the slit. Evaporation dynamics of a 20  $\mu\text{L}$  droplet under constant acoustic pressure on the MAM: temporal evolution of G) radius and contact angle, H) volume of the droplet captured for 1 h (60 min).

position on the slit, to tune the acoustic responses. We systematically investigate these droplet parameters for continuous spatial tuning of the acoustic wave. The contact angle and volume of droplet on the metamaterial can be modulated by electrowetting based droplet operations like merging,<sup>[46]</sup> mixing,<sup>[47]</sup> and splitting,<sup>[48]</sup> which are well-explored for numerous digital microfluidic platforms.<sup>[38]</sup>

#### 2.4.1. Effect of Droplet Volume

We perform distinct parametric study to realize the effect of droplet volume on the acoustic field modulation. We simulate 15 – 30  $\mu\text{L}$  droplet volumes (in step of 5  $\mu\text{L}$ ) placed at the left end to provide open slit aperture of 1.5 mm with the emission point at 1.5 mm and a constant droplet contact angle  $\approx 90^\circ$ . We observe that the transmitted acoustic field, measured over a

line 15 mm ( $\approx 1.74 \lambda$ ) above the substrate, follows exactly similar trends for all the droplet volumes as plotted in **Figure 5a**. This implies that we can achieve high fidelity for droplet volumes in the optimum range of 15 to 30  $\mu\text{L}$ . For droplets volume below 15  $\mu\text{L}$ , we observe significant droplet evaporation with time, and for larger volumes above 30  $\mu\text{L}$  volume other forces like gravity and inertia become significant and cannot be neglected.

#### 2.4.2. Effect of Droplet Contact Angle

We further study the field transmission for different droplet contact angles ( $\theta_a$ ) ranging from  $70^\circ$  to  $120^\circ$  for constant droplet position on the slit, implying a constant droplet radius ( $R$ ) but different droplet volumes ( $V$ ). The conservation of volume relates the droplet parameters as  $V = \frac{\pi R^3}{3} \{2 - 3 \cos \theta_a + \cos^3 \theta_a\}$ .

We observe that the variation in the transmitted acoustic field with the droplet contact angle becomes insignificant for droplet contact angles greater than  $70^\circ$ , as shown in the Figure 5b. It is difficult to move a droplet with contact angle less than  $70^\circ$  using electrowetting, because the change in the contact angle with the voltage reduces.<sup>[49,50]</sup> The contact angle reduction with increase in voltage is governed by Young Lipmann equation, however, beyond a threshold peak voltage and corresponding minimum angle, the contact angle become independent of the applied voltage, a phenomenon called contact angle saturation.<sup>[51]</sup> Thus, beyond a minimum-most angle, the droplet motion is limited by contact angle saturation.<sup>[52]</sup> Thus, the transmitted acoustic field can be manipulated with a systematic control and sustainability by managing the variable tunable parameters like the position of the droplet on the slit, an optimum droplet volume ( $15 - 30 \mu\text{L}$ ) and adequate droplet contact angle.

### 2.4.3. Effect of Evaporation

The droplet evaporation in the acoustic field for the duration of experiments ( $\approx 15\text{--}20$  min) seems negligible (see Figure 5C–F). However, to quantify droplet evaporation, we capture and measure the droplet radius and contact angle under constant acoustic pressure (Video S3, Supporting Information, recorded at 40 000 fps from a high-speed camera, and the ambient temperature is  $\approx 20^\circ\text{C}$  for the experiments). We observe the change in radius to be  $0.02 \pm 0.01$  mm and change in contact angle to be  $9^\circ \pm 2^\circ$  for initial 15 min, which turns out to be  $2.5 \pm 0.5 \mu\text{L}$  in volume. The plot for temporal evolution of droplet radius and contact angle is shown in Figure 5G,H. We observe a change in droplet contact angle, but no significant change in droplet radius for initial 15–30 min. The contact angle of the droplet remains well above  $70^\circ$ , and the transmitted acoustic pressure is nearly invariable for all angles greater than  $70^\circ$  (Figure 5B). It shows that evaporation will not impact the pressure dynamics for the time duration of the experiment, that is, 15–20 min. The average contact angle of the droplet on the slit is observed to be near  $90^\circ$  during continuous exposure of acoustic pressure for about one hour. However, to maintain the device operation for longer durations (more than 30 min), we need to resupply the droplet from a reservoir. The liquid reservoir can be easily built on the metasurface, as seen in numerous other works like lab-on-a-chip applications.<sup>[20,53]</sup> Electrowetting technique has been well-established for more than a decade now to merge, move, and manipulate droplets on open chip,<sup>[37,38]</sup> and since the metamaterial is based on droplet manipulation using electrowetting, thereby we can easily manipulate the volume of the droplet through merging, spitting, and moving. Thus, the device design not only takes the droplet evaporation in account, but it also provides the opportunity to tune the metamaterial on demand, by providing the liquid “on-demand” at the required point.

An oil surrounding or outer layer like in compound droplets<sup>[54]</sup> can also be used to prevent evaporation, however, numerous fluid properties like surface tension, impedance, evaporation rate, and viscosity need to be considered. The oscillation of the droplet under constant acoustic pressure is also analyzed by recording the droplet behavior over the slit at the

frame rate of 3000–100 000 fps. However, we do not observe any interface oscillation for the kHz acoustic frequencies (see Video S3, Supporting Information, recorded at 40 000 fps from a high-speed camera).

## 2.5. Broadband Dynamics

We study MAM broadband dynamics and observe that the MAM affects the spatial distribution of acoustic waves for 35–45 kHz broadband ultrasonic frequency spectrum.

We obtain similar binary switching for all frequencies 35–45 kHz by moving a deionized water droplet ( $25 \mu\text{L}$ ,  $90^\circ$ ) measured from 15 mm ( $\approx 1.74\lambda$ ) above the substrate as shown in Figure 6A. The corresponding simulations are in close agreement with the experimental results. The transmitted sound amplitude decreases by  $\approx 20$  dB when the droplet covers the slit, revealing MAM as a broadband tunable acoustic switch. We renormalized the measured data by calculating the pressure (dB) field with the device and normalizing it to the maximum value of the pressure (dB) field without any device for different acoustic frequencies. This was done because the source transducer had a resonance frequency of 40 kHz, thus, we obtained lower transmission for other frequencies (35 or 45 kHz). The normalized dB values provide better comparison for 35–45 kHz acoustic frequencies plotted together.

Similar broadband study is conducted with a droplet ( $20 \mu\text{L}$ ,  $90^\circ$ ) covering 2.5 mm of slit length for 35, 40, and 45 kHz frequencies. The measured and simulated normalized acoustic pressure over an acoustic axis (length 10 mm, slit center at 5 mm) (Figure 6B) show that the transmission coefficient of the field is greater than 0.8 (80%) and spatial distribution of acoustic pressure field was modulated by changing the open slit aperture with the droplet. The COMSOL simulation data have also been renormalized to match the measured data for no droplet case, for better comparison between the measured and simulated data for the droplet on the slit case.

The acoustic phase can also be modulated in a similar fashion for 35–45 kHz broad spectrum. We further simulate a  $15 \mu\text{L}$  droplet (center) motion from  $-2.5$  to  $2.5$  mm along the slit length, in step of 1 mm, to alter the open slit aperture (slit center is at 0 mm position). The phase maps for six different droplet positions on the slit are plotted in Figure 6C. These illustrates that the spatial wave-phase can be actively tuned from  $-\pi$  to  $+\pi$  by manipulating the effective location of the source. The phase values at a point  $(x,z) \approx (-11 \text{ mm}, 0 \text{ mm})$ , as marked on the phase maps, is also plotted for different emission points in Figure 6D for 35–45 kHz broad wave spectrum. The peak phase values, calculated over a line 15 mm ( $\approx 1.74 \lambda$ ) above the substrate for different frequencies, does not show any variation with the aperture width or width of the source as shown in Figure 6E.

## 3. Conclusion

Our work thus demonstrates a deep sub-wavelength ultrathin ( $200 \mu\text{m}$  in thickness, up to  $\lambda/44$ ) MAM, which for the first time to the best of author’s knowledge, has achieved active



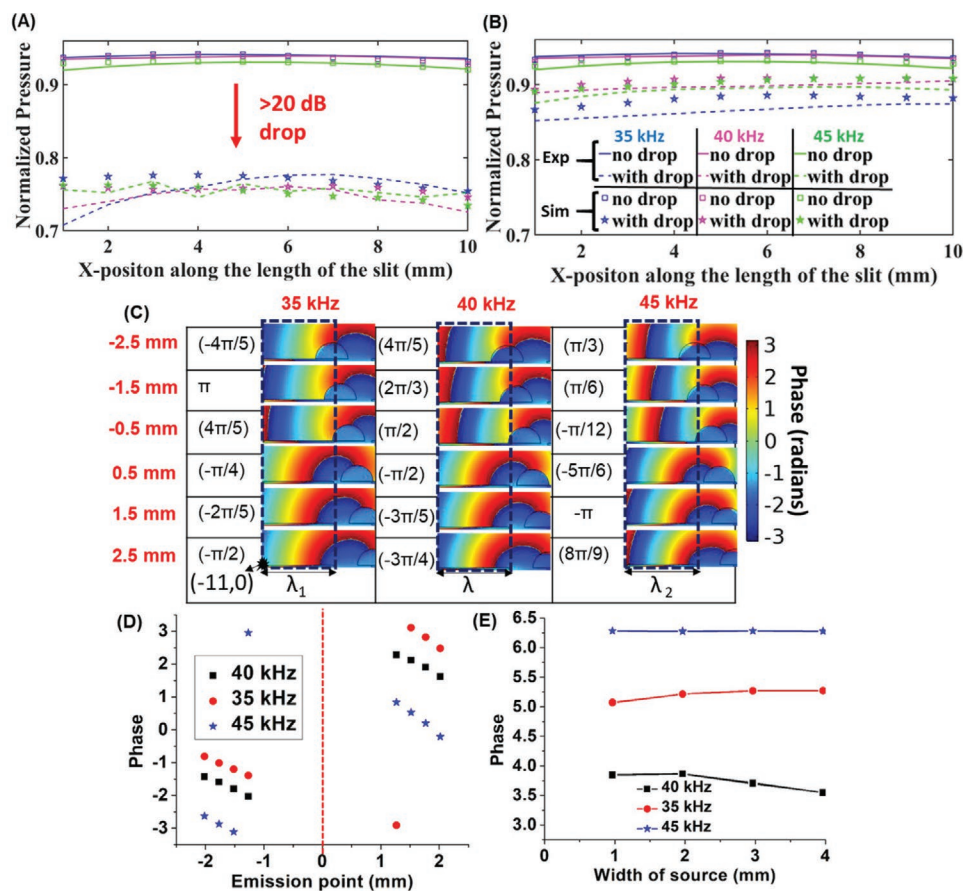


**Figure 6.** Broadband dynamics of MAM. Measured and simulated normalized acoustic pressure profiles are plotted along slit length ( $x$ -axis, i.e., 10 mm line along slit length with the slit center at  $x = 5$  mm) A) without and with the droplet on the slit for different frequencies (namely, 35, 40, and 45 kHz); B) without and with a droplet (20  $\mu$ L) at left end of the slit (width of the source  $\approx 2$  mm, emission point  $\approx 1.2$  mm) for different acoustic frequencies. C) The simulated phase map for 35–45 kHz acoustic frequencies plotting the transition in phase with different droplet positions on the slit. Droplet center is moving from  $-2.5$  to  $2.5$  mm along slit length in steps of 1 mm. The phase values at a point (shown by black star marked on one phase map)  $(x, z) \approx (-11, 0)$  is put in brackets adjacent to the phase maps for different acoustic frequencies. The dotted black rectangle marks the acoustic wavelengths ( $\lambda_1$ ,  $\lambda$ ,  $\lambda_2$ ). D) Simulated acoustic phase, for 35–45 kHz broad wave spectrum, plotted for a point  $(x, z) \approx (-11 \text{ mm}, 0 \text{ mm})$  varies from  $-\pi$  to  $+\pi$  with different emission points, attained when a 15  $\mu$ L droplet moves to cover different positions on the slit as mentioned in (C). The dotted red line marks the center of the slit. E) The peak phase value calculated on a line ( $1.74 \lambda$  above the slit) for different open slit apertures or width of the source.

tunability with high transmittance ( $>80\%$ ) at an ultra-compact device scale for 35–45 kHz acoustic frequencies by utilizing EWOD technique and MEMS actuation. MAM is a lightweight, broadband ultrasonic (35–45 kHz), low loss, and portable metamaterial with versatile functionalities ranging from on-demand ON/OFF switching and spatial amplitude modulation to tunable phase modulation for acoustic wave engineering. The integration of active microfluidic actuation techniques in liquid embedded metamaterial designs opens up new paradigms to achieve active tunability using many existing fluidic and MEMS techniques like electrophoresis, photo-electrowetting, and many more, which have never been utilized in acoustic metamaterials.<sup>[55]</sup> We conceptualized the metamaterial using a single slit and droplet, with variable control parameters like droplet contact angle, volume, position on the slit, and different electrode designs. We also established the broadband operations of MAM for 10 kHz wide range. Future research can deal with exploring different arrangements of multiple droplets and slits in rotated, spiral, or complex configurations by quantizing, modeling, and

multiplexing the parameters,<sup>[56–58]</sup> to render complex metamaterial operations such as beam forming and steering<sup>[59]</sup> and performing mathematical operations.<sup>[60]</sup> To achieve active actuation mechanism, many different challenges and parameters need to be considered like designing the electrode arrangement for multiple slits each with individual control circuitry for single or multiple droplet actuation, optimizing distance between slits, inter-electrode spacing, slit alignment (rectangular or circular array), pressure field and interference modeling, designing contact pads and wire connection (on surface or through via) for each electrode set fabricated with each slit, voltage actuation, and control for multiple droplets. The slit depth and shape can also be varied to observe resonant modes, which has been shown for extraordinary acoustic transmission from perforated plates and sub-wavelength slits.<sup>[61–63]</sup> Recently, a passive meta-surface lens has been demonstrated using deep sub-wavelength slits,<sup>[41]</sup> which imply the suitability of MAM for dynamic lensing and beam steering by the dynamic tunability. The transparency of the liquid and active tunability achievable

using MEMS and microfluidics approach, also allows to integrate both the acoustic and opto-fluidic metamaterial designs together, thereby opening unexplored dimensions to build next generation acousto-opto-microfluidic metamaterials.

## 4. Experimental Section

**Fabrication Method:** The devices were fabricated on ITO (130 nm) coated PET substrates (Sigma Aldrich). The facile fabrication of the slit on PET substrate was done using a laser cutter (VLS230), which had a resolution of 0.1 mm. The cleanroom fabrication facility was used to fabricate EWOD devices on the PET substrate.

The process flow schematic for fabrication is shown in Figure 1D, and the corresponding experimental video is shown in Video S2, Supporting Information. The devices were fabricated on ITO (130 nm) coated PET substrates (Sigma Aldrich) (Figure 1D (a)). ITO is a transparent and conductive metal used here to make electrodes. The facile fabrication of the slit on the PET substrate was done using a laser cutter (VLS230), which had a resolution of 0.1 mm (Figure 1D (b)). The cleanroom fabrication facility was used to fabricate EWOD devices surrounding the slit on the PET substrate. Initially, ITO metal electrodes were patterned using photolithography (Figure 1D (c)). For the lithography process, AZ1518 positive photoresist was spin coated at 4000 rpm for 40 s. Subsequently, the sample was soft baked at 110 °C for 50 s and then placed for UV exposure. The positive photoresist degraded at the exposed region and was removed through a developer. A Microposit developer was used to develop the positive resist for ≈20 s. The sample was hard baked for 1 min. After photolithography, the masked ITO layer was etched using hydrochloric acid (32% dilution) for 5–10 s (Figure 1D (d)). Then, the photoresist mask was stripped using an acetone dip (Figure 1D (e)). Subsequently, a dielectric layer of SU8 negative photoresist was coated at the top (Figure 1D (f)). SU8 2002 was spin coated at 3000 rpm for 30 s to give a thickness of 2 μm. The SU-8 layer was hard baked at 95 °C for 10 min. One more layer of dielectric SU8 2002 was spin coated for increasing the thickness to prevent dielectric breakdown and pinholes which cause electrolysis. The sample was subsequently heated at 95 °C for 10 min. Further, Teflon was spin coated at 4000 rpm for 40 s on the top. It was hard baked at 150 °C for 15 min. It formed the top-most hydrophobic layer to reduce hysteresis and promoted smoother droplet motion. The electrode designs are explained in the Supporting Information.

**Numerical Simulations:** Acoustic field 3D numerical simulations were carried out by the finite element solver in commercial software COMSOL Multiphysics v5.4. “Pressure Acoustics, Frequency Domain” module was used to see the sound dynamics in a 3D spherical space. Extremely fine physics based triangular mesh was used in the study on full domain except the PML. A plane wave radiation was used as the input. Pressure acoustics were modeled for both air (surrounding medium) and water with density being 1.2 and 1000 kg m<sup>-3</sup>, respectively, and speed of sound being 343 and 1481 m s<sup>-1</sup>, respectively. A perfectly matched boundary layer condition was imposed on the outer spherical boundaries of the simulation domain to prevent reflections and interference.

**Electrowetting Procedure:** A liquid droplet (volume 15–30 μL, with deposition tolerance ±1 μL) was placed on the slit using a micropipette. The contact angle of the droplet was around 90° ± 3°. A constant DC voltage with amplitude 150 V was used for the actuation. Since both the ground and voltage electrodes were covered by the dielectric layer, the dielectric thickness was doubled, thus, the effective voltage difference between the electrodes reduced to 106 V. The actuation voltage was generated using a combination of DC power supplies in series. The droplet was placed to be in contact with the adjacent electrodes on either side of the slit. As the field was turned ON, the droplet spread in the direction of electric field. As the applied field was turned OFF, that is, in absence of the electrowetting force, the actuated interface retracted to a more hemi-spherical state to conserve surface energy. Thus, the droplet was actuated and moved by sequential actuation of

the patterned electrodes on either side of the slit (Video S1, Supporting Information enclosed). Videos were recorded using a synchronized USB magnification endoscope (Digital Microscope, SOSENSE) and high-speed camera.

**Image Analysis:** The videos of the droplet motion using electrowetting (top-view) and static droplet in sound pressure (side-view) were recorded using a USB magnification endoscope (Digital Microscope, SOSENSE) and high-speed camera, respectively. Images were extracted from the recorded videos using MATLAB and Adobe Photoshop. Static droplet oscillations were also captured at 40 kHz acoustic pressure using a high-speed camera (Photron FASTCAM Nova S6 type 800K-M-32GB) with a Macro (1:1) lens (TAMRON AF 90 mm F/2.8), however, any noticeable deformation was not seen even at 100 000 fps.

**Transmission and Field Mapping Measurements:** Transmission amplitude was measured by mounting an acoustic source of 40 kHz transducer (MA40S4S, Murata Electronics, Japan) below the substrate. The transducer had a beam spread angle of ±40° and sound pressure levels of 120 ± 3 dB (measured on the axis at z ≈ 30 cm). The transducer was driven using 20 Vpp sinusoidal voltage signal at 40 kHz frequency, generated using a GW INSTEK AFG-2225 Dual-channel arbitrary function generator. Quantitative pressure measurements were obtained using a calibrated Brüel & Kjaer microphone (model 4138-A-015) positioned 15 mm and higher above the MAM device. A 3D linear stage was built in the laboratory for scanning the 3D space. The signal received from the microphone was amplified using a mic preamp: Brüel & Kjaer 2670 and a 1-channel Microphone Conditioning Amplifier 2690-A-0S1. The signals were sent to a PicoScope 4262 oscilloscope to record the differences between the received and reference input driving signals, which were used for calculating the phase of the acoustic waves. MATLAB was used to plot the captured data for the acoustic pressure amplitude and phase maps. The transmitted normalized pressure was calculated as  $P(\text{dB}) = 20 \log\left(\frac{P_m}{P_0}\right)$ , where  $P_m$  and  $P_0$  (≈10<sup>-5</sup> Pa) are the measured and reference acoustic pressures respectively. Please note for all the plotted pressure and phase measurements, the slit center was at the center of x-axis and y-axis on the graphs, and all the measurements were taken at 15 mm (≈1.74 λ) above the substrate, that is, it corresponds to z = 0 mm for x–z plane.

## Supporting Information

Supporting Information is available from the Wiley Online Library or from the author.

## Acknowledgements

This work was supported by the EU-H2020 through their ERC Advanced Grant (number 787413) and the Royal Academy of Engineering through their Chairs in Emerging Technology Program (CIET18/19). The authors would like to thank Prof. Bruce W Drinkwater for his valuable inputs and support in this work. The authors acknowledge Mr. Eimontas Jankauskis for his help in capturing videos and making schematics for this work.

## Conflict of Interest

The authors declare no conflict of interest.

## Data Availability Statement

The data that support the findings of this study are available from the corresponding author upon reasonable request.

## Keywords

acoustic metamaterials, electrowetting-on-dielectric, microfluidics, tunability

Received: April 27, 2021  
Revised: June 11, 2021  
Published online:

- [1] S. A. Cummer, J. Christensen, A. Alù, *Nat. Rev. Mater.* **2016**, *1*, 16001.
- [2] G. Ma, P. Sheng, *Sci. Adv.* **2016**, *2*, e1501595.
- [3] N. Fang, D. Xi, J. Xu, M. Ambati, W. Srituravanich, C. Sun, X. Zhang, *Nat. Mater.* **2006**, *5*, 452.
- [4] Y. Li, M. B. Assour, *Sci. Rep.* **2015**, *5*, 17612.
- [5] Y. Xie, W. Wang, H. Chen, A. Konneker, B.-I. Popa, S. A. Cummer, *Nat. Commun.* **2014**, *5*, 5553.
- [6] X. Zhu, K. Li, P. Zhang, J. Zhu, J. Zhang, C. Tian, S. Liu, *Nat. Commun.* **2016**, *7*, 11731.
- [7] R. Al Jahdali, Y. Wu, *Appl. Phys. Lett.* **2016**, *108*, 031902.
- [8] J. Mei, Y. Wu, *New J. Phys.* **2014**, *16*, 123007
- [9] F. Zangeneh-Nejad, R. Fleury, *Rev. Phys.* **2019**, *4*, 100031.
- [10] S. Chen, Y. Fan, Q. Fu, H. Wu, Y. Jin, J. Zheng, F. Zhang, *Applied Sciences* **2018**, *8*, 1480.
- [11] B. I. Popa, D. Shinde, A. Konneker, S. A. Cummer, *Phys. Rev. B: Condens. Matter Mater. Phys.* **2015**, *91*, 220303.
- [12] B. I. Popa, S. A. Cummer, *Nat. Commun.* **2014**, *5*, 3398.
- [13] L. Airoidi, M. Ruzzene, *New J. Phys.* **2011**, *13*, 113010.
- [14] F. Casadei, T. Delpero, A. Bergamini, P. Ermanni, M. Ruzzene, *J. Appl. Phys.* **2012**, *112*, 064902.
- [15] R. L. Lincoln, F. Scarpa, V. P. Ting, R. S. Trask, *Multifunct. Mater.* **2019**, *2*, 043001.
- [16] P. Wang, F. Casadei, S. Shan, J. C. Weaver, K. Bertoldi, *Phys. Rev. Lett.* **2014**, *113*, 014301.
- [17] S. Xiao, G. Ma, Y. Li, Z. Yang, P. Sheng, *Appl. Phys. Lett.* **2015**, *106*, 091904.
- [18] Z. Tian, C. Shen, J. Li, E. Reit, Y. Gu, H. Fu, S. A. Cummer, T. J. Huang, *Adv. Funct. Mater.* **2019**, *29*, 1808489.
- [19] N. T. Nguyen, M. Hejazian, C. H. Ooi, N. Kashaninejad, *Micromachines* **2017**, *8*, 186.
- [20] S. Haeberle, D. Mark, F. Von Stetten, R. Zengerle, in *Microsystems and Nanotechnology*, Springer, Berlin **2012**, p. 853.
- [21] A. M. Watson, A. B. Cook, C. E. Tabor, *Adv. Eng. Mater.* **2019**, *21*, 1900397.
- [22] K. Mishra, C. Murade, B. Carreel, I. Roghair, J. M. Oh, G. Manukyan, D. Van Den Ende, F. Mugele, *Sci. Rep.* **2014**, *4*, 6378.
- [23] J. Friend, L. Y. Yeo, *Rev. Mod. Phys.* **2011**, *83*, 647.
- [24] S. P. Zhang, J. Lata, C. Chen, J. Mai, F. Guo, Z. Tian, L. Ren, Z. Mao, P. H. Huang, P. Li, S. Yang, T. J. Huang, *Nat. Commun.* **2018**, *9*, 2928.
- [25] W. Connacher, N. Zhang, A. Huang, J. Mei, S. Zhang, T. Gopesh, J. Friend, *Lab Chip* **2018**, *18*, 1952.
- [26] G. Destgeer, H. J. Sung, *Lab Chip* **2015**, *15*, 2722.
- [27] Y.-P. Zhao, Y. Wang, *Rev. Adhes. Adhes.* **2013**, *1*, 114.
- [28] F. Mugele, J.-C. Baret, *J. Phys.: Condens. Matter* **2005**, *17*, R705.
- [29] W. C. Nelson, C. C. J. Kim, *J. Adhes. Sci. Technol.* **2012**, *26*, 1747.
- [30] H. Tang, Z. Chen, N. Tang, S. Li, Y. Shen, Y. Peng, X. Zhu, J. Zang, *Adv. Funct. Mater.* **2018**, *28*, 1801127.
- [31] Y. X. Shen, Y. G. Peng, F. Cai, K. Huang, D. G. Zhao, C. W. Qiu, H. Zheng, X. F. Zhu, *Nat. Commun.* **2019**, *10*, 3411.
- [32] N. Trompette, J.-L. Barbry, F. Sgard, H. Nelisse, *J. Acoust. Soc. Am.* **2009**, *125*, 31.
- [33] F. P. Mechel, *J. Sound Vib.* **1986**, *111*, 297.
- [34] Z. Ma, K. Melde, A. G. Athanassiadis, M. Schau, H. Richter, T. Qiu, P. Fischer, *Nat. Commun.* **2020**, *11*, 4537.
- [35] L. Tong, Z. Xiong, Y. X. Shen, Y. G. Peng, X. Y. Huang, L. Ye, M. Tang, F. Y. Cai, H. R. Zheng, J. Bin Xu, G. J. Cheng, X. F. Zhu, *Adv. Mater.* **2020**, *32*, 2070276.
- [36] E. Bok, J. J. Park, H. Choi, C. K. Han, O. B. Wright, S. H. Lee, *Phys. Rev. Lett.* **2018**, *120*, 44302.
- [37] S. Y. Teh, R. Lin, L. H. Hung, A. P. Lee, *Lab Chip* **2008**, *8*, 198.
- [38] S. K. Cho, H. Moon, C.-J. Kim, *J. Microelectromech. Syst.* **2003**, *12*, 70.
- [39] R. Ghaffarivardavagh, J. Nikolajczyk, R. Glynn Holt, S. Anderson, X. Zhang, *Nat. Commun.* **2018**, *9*, 1349.
- [40] H. L. Zhang, Y. F. Zhu, B. Liang, J. Yang, J. Yang, J. C. Cheng, *Appl. Phys. Lett.* **2017**, *111*, 203502.
- [41] J. Chen, J. Xiao, D. Lisevych, A. Shakouri, Z. Fan, *Nat. Commun.* **2018**, *9*, 4920.
- [42] M. M. Nahar, J. B. Nikapitiya, S. M. You, H. Moon, *Micromachines* **2016**, *7*, 71.
- [43] Y. Xie, C. Shen, W. Wang, J. Li, D. Suo, B. I. Popa, Y. Jing, S. A. Cummer, *Sci. Rep.* **2016**, *6*, 35437.
- [44] S. Laureti, D. A. Hutchins, L. A. J. Davis, S. J. Leigh, M. Ricci, *AIP Adv.* **2016**, *6*, 121701.
- [45] F. , Sun, S. Guo, B. Li, Y. Liu, S. He, *Acoust. Phys.* **2019**, *65*, 1.
- [46] S. Bansal, P. Sen, *J. Colloid Interface Sci.* **2018**, *530*, 223.
- [47] S. Bansal, P. Sen, *Sens. Actuators, B.* **2016**, *232*, 318.
- [48] N. Y. J. B. Nikapitiya, M. M. Nahar, H. Moon, *Micro Nanosyst. Lett.* **2017**, *5*, 24.
- [49] F. Mugele, J. C. Baret, *J. Phys.: Condens. Matter* **2005**, *17*, R705.
- [50] Y. Guan, B. Li, M. Zhu, S. Cheng, J. Tu, *Phys. Fluids* **2019**, *31*, 062002.
- [51] A. Quinn, R. Sedev, J. Ralston, *J. Phys. Chem. B* **2005**, *109*, 6268.
- [52] H. A. A. Ali, H. A. Mohamed, M. Abdelgawad, *Biomicrofluidics* **2015**, *9*, 014115.
- [53] R. B. Fair, *Microfluid. Nanofluid.* **2007**, *3*, 245.
- [54] S. Bansal, P. Sen, *Langmuir* **2017**, *33*, 11047.
- [55] C. Choi, S. Bansal, N. Münzenrieder, S. Subramanian, *Adv. Eng. Mater.* **2020**, *23*, 2170008.
- [56] G. Memoli, M. Caleap, M. Asakawa, D. R. Sahoo, B. W. Drinkwater, S. Subramanian, *Nat. Commun.* **2017**, *8*, 14608.
- [57] K. H. Matlack, M. Serra-Garcia, A. Palermo, S. D. Huber, C. Daraio, *Nat. Mater.* **2018**, *17*, 323.
- [58] C. Della Giovampaola, N. Engheta, *Nat. Mater.* **2014**, *13*, 1115.
- [59] O. T. Von Ramm, S. W. Smith, *IEEE Trans. Biomed. Eng.* **1983**, *BME-30*, 438.
- [60] A. Silva, F. Monticone, G. Castaldi, V. Galdi, A. Alù, N. Engheta, *Science* **2014**, *343*, 160.
- [61] M. H. Lu, X. K. Liu, L. Feng, J. Li, C. P. Huang, Y. F. Chen, Y. Y. Zhu, S. N. Zhu, N. Ben Ming, *Phys. Rev. Lett.* **2007**, *99*, 174301.
- [62] C. Rubio, A. Uris, P. Candelas, F. Belmar, V. Gomez-Lozano, *AIP Adv.* **2015**, *5*, 057150.
- [63] H. Estrada, P. Candelas, A. Uris, F. Belmar, F. Meseguer, F. J. Garcia De Abajo, *Appl. Phys. Lett.* **2008**, *93*, 011907.